Paper ID ILASS08-1-17

ILASS 2008
Sep. 8-10, 2008, Como Lake, Italy

NUMERICAL SIMULATION OF ATOMIZATION WITH ADAPTIVE JET REFINEMENT

Anne Bagué*, Daniel Fuster*, Stéphane Popinet+ & Stéphane Zaleski*

*Université Pierre et Marie Curie, UMR-CNRS 7190, Institut Jean Le Rond D'Alembert
4 Place Jussieu case 162, Paris cedex 05, 75252, France

+National Institute of Water and Atmospheric Research
P.O. Box 14-901, Kilbirnie, Wellington, New Zealand

bague@lmm.jussieu.fr, fuster@lmm.jussieu.fr

ABSTRACT
Atomization processes occur in different systems like engine injectors. When a liquid is injected with a surrounding gas, small instabilities appear at the interface. When their amplitude is small enough, a linear instability appears and the problem can be solved in two dimensions with the Orr-Sommerfield equation. The temporal shear instability for two-phase laminar flow is studied for two different cases. The validity of the results obtained from the temporal theory applied to the spatial-temporal problem is also investigated.

Atomization processes occur in numerous industrials fields. For example, in engine injectors, fuel is atomized into droplets when injected inside the combustion chamber in a complex process. Using simulation techniques it is possible to estimate the combustion quality, the engine efficiency and pollution rate.

When a liquid jet is atomized, a strong interaction is produced between the jet and the surrounding gas and, depending on gas and liquid properties and the injector nozzle geometry, an instability appears. The fluctuations introduced in the mean flow are responsible for the appearance of small disturbances which, initially, display a linear behavior. When these perturbations grow downstream they originate thin ligaments which eventually break into droplets.

This paper focuses on the simulation of the linear stability of shear for two-phase mixing layer flows in two dimensions and the analysis of the instability produced in the primary atomization.

To perform the simulations, a numerical code based on Volume of Fluid (VOF) advection scheme for interfacial flows is used (GERRIS, http://gfs.sf.net). GERRIS [5] is an adaptative mesh refinement code for the time-dependent incompressible Navier-Stokes equations with a multigrid solver. The method is based on quad/octree spatial discretization with automatic and dynamic local refinement. The pressure is obtained by means of a multilevel Poisson solver. Continuous surface force (CSF) is used with the height function method [3] to model surface tension [4].

1 LINEAR STABILITY

When a liquid is atomized with a surrounding gas, analysis of the evolution of the small instabilities introduced in the flow can be done with the aid of linear theory applied to two-phase mixing layer. In particular, the theoretical solutions of this linear problem can be obtained by solving the Orr-Sommerfield equation.

1.1 Theory

Let us consider a domain defined by $-L_l < y < 0$ for the liquid phase and $0 < y < L_g$ for the gas phase. The following properties ratios are defined: the density $r = \rho_g/\rho_l$, the viscosity $m = \mu_g/\mu_l$ and boundary layer thickness in the two fluids profiles $n = \delta_g/\delta_l$ with the initial velocities profiles given by (Figure 1):

$$U_l(y) = U_{int} - U_l^* erf\left(y/\delta_l\right), \quad (1)$$

$$U_g(y) = U_{int} + U_g^* erf\left(y/\delta_g\right). \quad (2)$$

where U_{int} is the interface velocity and U^* is:

$$\begin{cases} U_l^* = U_{int} - U_l, \\ U_g^* = U_g - U_{int}. \end{cases} \quad (3)$$

For this case, it has been decided to use a system of reference moving with the interface and therefore, U_{int} equals to zero.

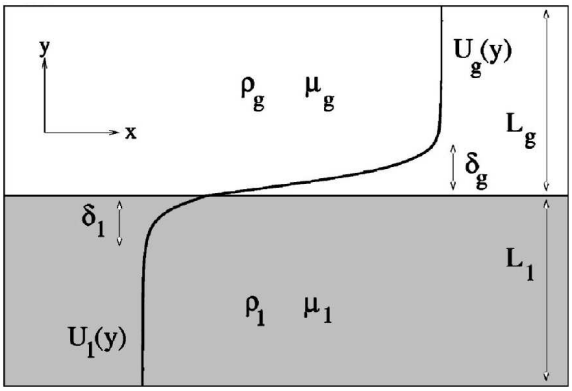

Figure 1: Parameters and profiles used for the liquid and gas phases.

A relation between these parameters can be obtained by applying the stress continuity condition:

$$\frac{U_g^*}{U_l^*} = \frac{n}{m}. \tag{4}$$

In order to interpret the results, it is useful to define the following Reynolds and Weber numbers. These dimensionless numbers will have an important effect on the type of observed instabilities [1]:

$$\begin{aligned} Re_l &= \tfrac{\rho_l\ U_g^*\ \delta_g}{\mu_l}, \quad Re_g = \tfrac{\rho_g\ U_g^*\ \delta_g}{\mu_g}, \\ We_l &= \tfrac{\rho_l\ (U_g^*)^2\ \delta_g}{\sigma}. \quad We_g = \tfrac{\rho_g\ (U_g^*)^2\ \delta_g}{\sigma}. \end{aligned} \tag{5}$$

The Orr-Sommerfield equation takes into account the perturbation streamfunctions ψ_g and ψ_l, defined in relation to streamwise and cross-stream velocity components u and v in both phases [6]:

$$u = \partial_y \psi_{l,g}, \qquad v = -\partial_x \psi_{l,g}. \tag{6}$$

The solutions are periodic in time and space:

$$\psi_{l,g} = \phi_{l,g}(y) e^{i\alpha(x-ct)}. \tag{7}$$

The complex wave speed c depends on the real wave number α. The perturbation equations for the liquid and the gas phase are [2]:

$$(U_l - c)\left(D^2 - \alpha^2\right)\phi_l - U_l''\phi_l = \frac{1}{i\alpha Re_l}\left(D^2 - \alpha^2\right)^2 \phi_l, \tag{8}$$

$$(U_g - c)\left(D^2 - \alpha^2\right)\phi_g - U_g''\phi_g = \frac{m}{r}\frac{1}{i\alpha Re_l}\left(D^2 - \alpha^2\right)^2 \phi_g. \tag{9}$$

where D is the differential operator for y.

At the edge of the domain, the following boundary conditions are imposed:

$$\phi_l = \phi_l' = 0 \quad \text{at} \quad y = -L_l, \tag{10}$$

$$\phi_g = \phi_g' = 0 \quad \text{at} \quad y = L_g. \tag{11}$$

At the interface, the normal and tangential continuity of velocity and of stress conditions are applied:

$$\phi_l' + \frac{U_l'\phi_l}{c} = \phi_g + \frac{U_g'\phi_g}{c}, \tag{12}$$

$$\phi_l = \phi_g, \tag{13}$$

$$\phi_l'' + \alpha^2\phi_l + \frac{U_l''\phi_l}{c} = m\left(\phi_g'' + \alpha^2\phi_g + \frac{U_g''\phi_g}{c}\right), \tag{14}$$

$$\begin{aligned} &\frac{1}{ir\alpha Re_l}\left(\phi_l''' - 3\alpha^2\phi_l'\right) + \frac{1}{r}\left(c\phi_l' + U_l'\phi_l\right) \\ &-\frac{m}{ir\alpha Re_l}\left(\phi_g''' - 3\alpha^2\phi_g'\right) - \left(c\phi_g' + U_g'\phi_g\right) = \frac{\alpha^2}{rcWe_l}\phi_l. \end{aligned} \tag{15}$$

1.2 Results

The examples used in this work for the code validation are summarized in Table 1.

reference	m	r	δ_l/L	δ_g/L
A	0.1	1	0.25	0.25
B	0.1	1	0.25	0.25
C	0.99	0.1	0.25	0.25
D	0.99	0.1	0.25	0.25

reference	Re_l	Re_g	We_l	We_g
A	200	2000	∞	∞
B	200	2000	10	10
C	19800	2000	∞	∞
D	19800	2000	100	10

Table 1: Characteristics of the simulations

For cases A and B ($m = 0.1$ and $r = 1$), the results are depicted in Figure 2.

The numerical results give a good approximation of the linear theory. Without surface tension, the mean error between numerical and theoretical results is $2.22\ \%$. When surface tension is included, the simulations give a better estimation of linear theory with a mean error of $0.80\ \%$.

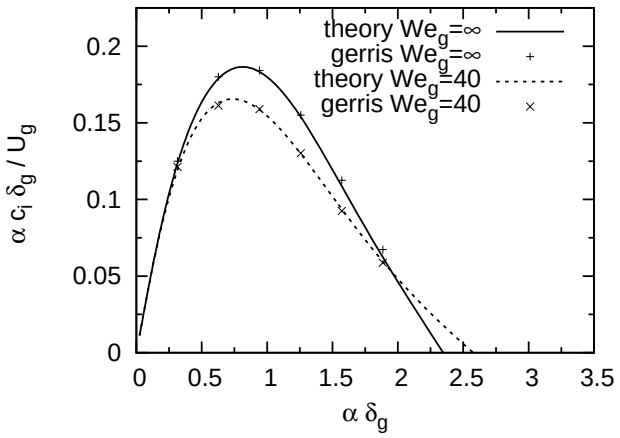

Figure 2: Growth rate of unstable modes and the corresponding results with GERRIS code for cases A and B from Table 1.

Figure 3 shows the numerical and theoretical curves when $m = 0.99$ and $r = 0.1$ (cases C and D).

An improved approximation is obtained compared to the previous results. The simulation results correctly predict the non-dimensionned growth rate αc_i provided by the linear theory. The mean error between numerical and theoretical results are 0.44 %, for the case without surface tension and 0.62 % with surface tension.

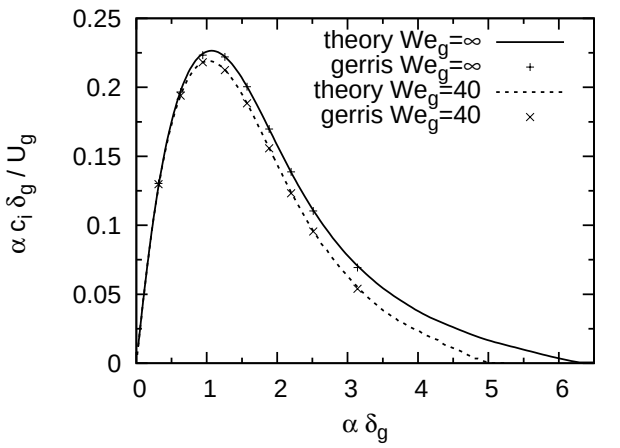

Figure 3: Growth rate of unstable modes and the corresponding results with GERRIS code for cases C and D the Table 1.

Results obtained with numerical simulations compare favorably with the theorerical solution obtained with the Orr-Sommerfield equation. The accuracy of the results is lower for case A. For a small vicosity ratio, slight differences are observed which become more appreciable for small density ratios.

Table 2 exhibits the percentage of the error between the theorical and numerical results are calculated for different mesh sizes.

reference	32	64	128	256
A	21.33	10.74	3.50	1.5
B	7.30	1.28	0.48	1.04
C	1.17	0.24	0.14	0.09
D	1.39	0.76	0.07	0.54

Table 2: Percentage of the error for the different cases from Table 1 and for mesh sizes of 32, 64, 128 and 256.

Generally, a better approach is obtained when the mesh is refined except when surface tension is included for the two most refine meshes. However, the error always remains close to 1 %.

The solutions obtained by the numerical code can therefore be considered as good approximations of the real solutions, and they will be used for the rest of this work to analyze the behavior of jets in more complex situations.

2 INSTABILITIES PRODUCED IN THE PRIMARY ATOMIZATION

In this section, the jet behavior in the primary atomization zone is investigated. High resolution simulations are used. The mesh is adapted in the zones where the solution is more complex, namely, at interfaces and vortices. The smallest mesh size is about $0.8\mu m$. Output boundary conditions are applied in all boundaries of the domain except at the entrance, where the velocity profile is prescribed according to Eq. (2) with an interface velocity defined by the stress condition at the interface (Eq. 4). Moreover, a perturbation v' is introduced in the vertical velocity, which is a random function applied either in the liquid or in the gas giving values inside the range $[-0.1\,U : 0.1\,U]$. The rest of conditions required for the simulation are included in Table 3, and the relevant dimensionless parameters of these simulations can be found in Table 4.

	U (m/s)	ρ (kg/m^3)	μ (Pa $\cdot$ s)
Liquid	20	1000	$5 \cdot 10^{-4}$
Gas	100	200	$1.7 \cdot 10^{-5}$

	σ (N/m)	Domain size (μm)	δ (μm)
Liquid	0.03	40	11.8
Gas		60	2.0

Table 3: Simulation conditions used for the analysis of the instabilities in the primary atomization zone.

m	r	δ_l/L	δ_g/L
0.034	0.200	0.118	0.200

Re_l	Re_g	We_l	We_g
400	2353	667	133

Table 4: Representative dimensionless numbers for the conditions included in Table 3.

Figure 4 displays a representative view of the behavior of the jet for the conditions indicated above. As it can be seen, the simulation domain is focused only in the primary atomization zone, before the jet is definitely broken into droplets.

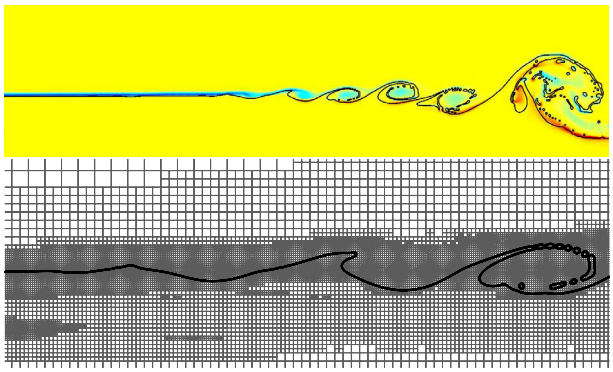

Figure 4: Interface profile along a distance of $400\mu\mathrm{m}$ downstream of the injector at $t = 50\mu\mathrm{s}$ (top). Zoom to the transition between the linear and non-linear regime (bottom).

Two main zones can be distinguished:

- In the first zone, the disturbances at the entrance generate small instabilities which are quickly amplified downstream. The intensity of the instabilities is measured using the kinetic turbulent energy. Figure 5 depicts this variable at different positions from the entrance. In the very early stage of injection the initial turbulence induced in the liquid is firstly transferred to the interface (transition from $x/\delta_g = 0$ to $x/\delta_g = 25$). Then, even when the small disturbances introduced at the entrance are quickly dissipated in the bulk liquid due to viscous effects, they are strong enough to create some instabilities at the interface.

  As the instabilities grow downstream, the level of turbulence inside the gas and liquid increases, mainly in zones near the interface. It can be stated that the small perturbation originally induced in the liquid is firstly transferred to the interface, which finally generates a strong turbulence downstream not only in the liquid, but also in the gas. Remarkably, this phenomenon is also encountered when the instabilities are induced in the gas (Figure 6). In this case, the gas momentum is powerful enough to generate appreciable perturbations at the interface, which are finally amplified producing a strong turbulence on both phases.

- In the second zone, the instabilities become nonlinear and ligaments appear. These ligaments are finally broken into droplets which interact with the vortex appearing in the gas phase near the interface. It has been found that for large Reynolds numbers, the flow structures in the gas vortex generated under the ligaments strongly interact with the drops which have been generated. Therefore, simulation results are extremely sensitive to the mesh size and DNS simulation of the jet is required, considerably restricting the Reynolds numbers which could be reached with a high degree of accuracy.

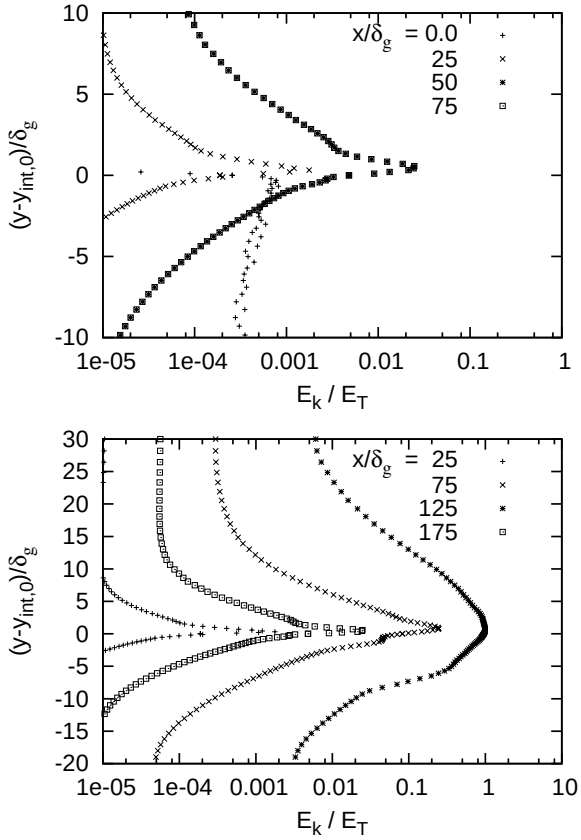

Figure 5: Profiles of the turbulent kinetic energy ($E_k = 1/2(u_i')^2$) at different distances from the injector. Perturbation is solely induced in the liquid phase.

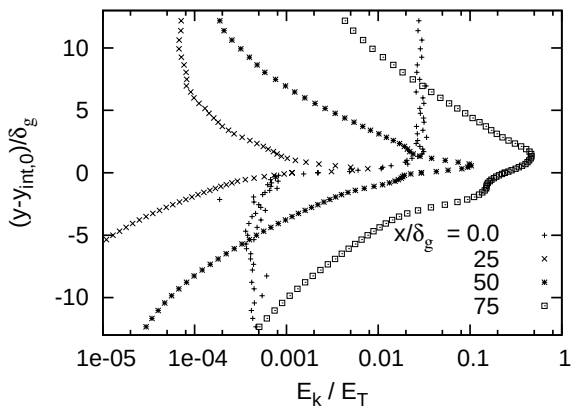

Figure 6: Profiles of the turbulent kinetic energy ($E_k = 1/2(u_i')^2$) at different distances from the injector. The perturbation is solely induced in the gas phase.

Thus, it can be concluded that turbulence at the entrance either of both phases is going to promote the appearance of instabilities at the interface, whose amplification is responsible for the transition from the linear to the nonlinear regime. This transition is captured in Figure 7, where the time-averaged maximum of the interface position at different locations is plotted as a function of the distance from the injector. During the first zone, a clear exponential growth is observed and once the amplitude of the waves is much larger than the thickness of the boundary layer, the growth rate is saturated.

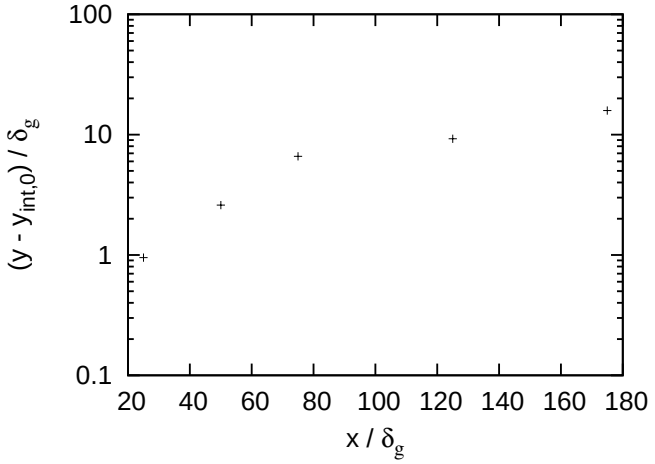

Figure 7: Evolution of the averaged amplitude of the waves along the jet. Transition to the linear regime with an exponential growth of the waves ($x/\delta_g \leq 80$) to the non-linear regime.

In the linear regime, this initial growth rate is a function of parameters like the Reynolds and Weber number or the gas and viscosity ratios. Some attempts have been done in order to use the linear theory to predict the characteristic frequencies which are going to be amplified downstream. However, the lack of a complete developed theory for the temporal-spatial problem and the difficulties related with the temporal change of the base flow makes it is necessary to resort to numerical simulations in order to investigate these type of situations. Nevertheless, it is interesting to compare some of the results from simulations with those obtained from the linear theory already presented in section 1.

Firstly, it is important to emphasize that numerical results are compared with theoretical results based on the assumption that the Gaster relation is applicable, which is just justified when the velocity of the waves is larger than the group velocity. This property is revealed by stopping the perturbation at the inlet. For the case studied here, the waves are then propagated downstream and the equilibrium state given by the input boundary conditions is recovered.

Another effect which should be taken into account is the evolution of the base flow downstream. The changes in the velocity profiles as well as those in the boundary layer thickness can alter the behavior of the different modes. Figure 8 depicts different velocity profiles at different positions downstream of the injector. Just in a very short distance from the entrance, the velocity profile is similar to that introduced as an input boundary condition. The boundary layer then grows due to viscous effects, and when the flow becomes nonlinear (for distances larger than $x/\delta_g = 80$) the velocity profile is significantly modified due to the turbulence generated for the waves.

For a more accurate comparison between simulation and theoretical results, four spectra at different locations are plotted in Figure 9. The interpretation of the results has to be understood under the following assumptions:

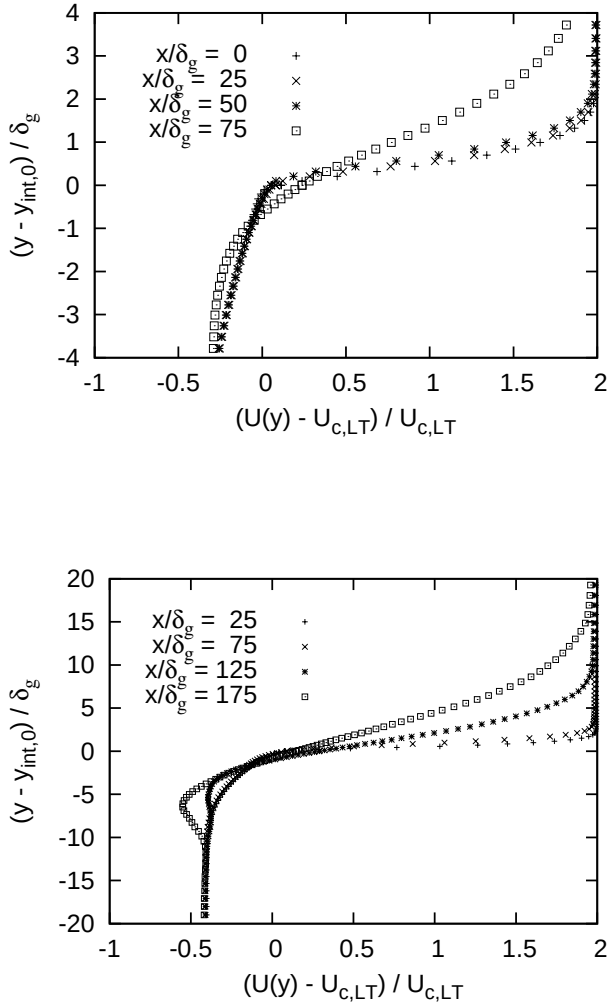

Figure 8: Evolution of the velocity profile and interface position in different sections. Top graph: Evolution of the velocity profile in the zone where waves are still linear. Bottom: Transition from the linear to the nonlinear zone.

- Due to the instability has been identified as convective, it is considered that some convective velocity relates the frequencies measured in the simulations, f, and the wavelenghts predicted by theory α. As a first approximation this velocity is taken as a constant and it is obtained from Eq. **??**.

- The Gaster relation is used to relate frequencies and wavelenghts:

$$U_{c,LT} = \frac{f}{\alpha} \tag{16}$$

- The initial perturbation amplitude is assumed to be equal for all the frequencies. Thus, the amplitude at some distance x from the injector would be proportional to the growthrate c_i.

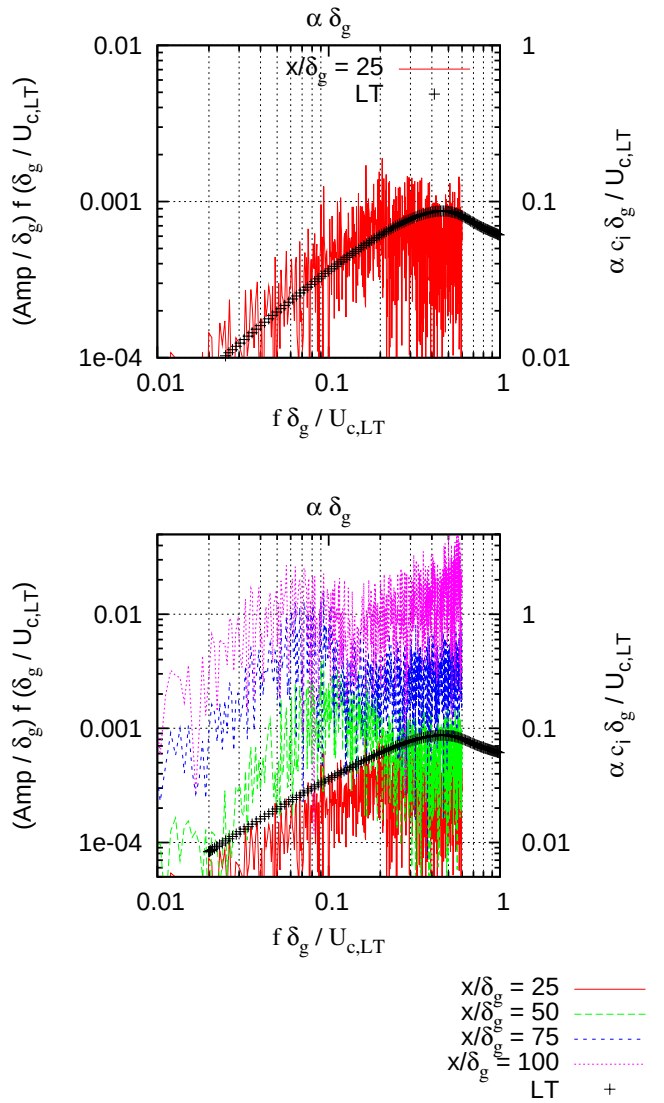

Figure 9: FFT of the temporal signal at different locations (lines) and theoretical growthrate (dots).

Despite the simplifications done to perform the comparison, a good fitting is displayed between the numerical and theoretical spectra. Results fit specially well for the first spectrum ($x/\delta_g = 25$), where the small instabilities are still linear. As explained, the most amplified frequencies tend to decrease downstream which is a consequence of the vortex growth in the two phase mixing boundary layer. When the instability is large enough, the vortex generated in the gas phase predominately excites low frequencies which become even smaller as the vortex grows downstream.

CONCLUSION

The temporal viscous linear theory in two dimensions for two-phase flow has been used to validate the numerical code. The adaptative mesh refinement code used in this work (GERRIS) correctly verifies the linear theory independently of the value of the surface tension.

The results provided by the linear theory have been shown to also correctly predict the main behavior of the instabilities in the primary atomization zone when the spatial-temporal is studied. GERRIS code has allowed us to observe the different instabilities created in this zone.

REFERENCES

[1] T. Boeck, J. Li, E. López-Pagés, P. Yecko & S. Zaleski, Ligament formation in sheared liquid–gas layers, *Theoretical and Computational Fluid Dynamics*, vol. 21, pp. 59-76, 2007.

[2] T. Boeck & S. Zaleski, Viscous versus inviscid instability of two-phase mixing layers with continuous velocity profile, *Phys. Fluids*, vol. 17, 032106, 2005.

[3] M. Francois, S. Cummins, E. Dendy, D. Kothe, J. Sicilian & M. Williams, A balanced-force algorithm for continuous and sharp interfacial surface tension models within a volume tracking framework, *J. Comput. Phys.*, vol. 213 (1), pp. 141-173, 2006.

[4] S. Popinet, An accurate adaptive solver for surface-tension-driven interfacial flows, *(In preparation)*.

[5] S. Popinet, Gerris: a tree-based adaptive solver for the incompressible Euler equations in complex geometries, *J. Comput. Phys.*, vol. 190,pp. 572-600, 2003.

[6] P. Yecko & S. Zaleski, Transient growth in two-phase mixing layers, *J. Fluid Mech.*, vol. 528,pp. 43-52, 2005.